Check for updates

LASER & PHOTONICS REVIEWS
www.lpr-journal.org

Single-Panel Complex Holographic Display with Three-Phase Covalent Macropixel

Yunhee Kim, Jonghyun Lee, Sehwan Na, Hoon Song, Soobin Kim, Hyeonseung Yu, Jungkwon Ahn, Chilseong Choi, Hongsuk Kim, Hong-Seok Lee, and Hwi Kim**

A single-panel complex holographic display with a three-phase covalent macropixel featuring ultralow noise and high-efficiency 3D image generation is proposed. The essential feature of the proposed three-phase covalent macropixel is the point-symmetric covalent concatenation of sub-pixels and an adaptive computer-generated hologram encoding algorithm. The proposed single-panel holographic display exhibits three times signal efficiency enhancement, 1/38 reduction of DC noise, and 1/50 reduction of conjugate noise compared to conventional holographic displays in the generation of full-color computer-generated hologram images. This noise reduction leads to three times the optical efficiency enhancement of holographic displays.

1. Introduction

Holographic 3D displays generate high-definition 3D object images in free space via spatial light modulation.[1–15] Complex spatial light modulation that is the simultaneous and independent modulation of the amplitude and phase of a full-color optical wave field is a prerequisite for achieving photorealistic holographic fields of 3D scenes. However, even in state-of-the-art holographic displays, complex spatial light modulation has yet to be adopted. As of now, complex spatial light modulator (SLM) technology in a flat-panel form remains unrealized.

Y. Kim, H. Song, H. Yu, J. Ahn, C. Choi, H. Kim
Samsung Electronics
34, Seongchon-gil, Seoul, Seocho-Gu 06765, Republic of Korea
J. Lee, S. Na, S. Kim, H. Kim
Department of Electronics and Information Engineering
Korea University
2511, Sejong-ro, Sejong 30019, Republic of Korea
E-mail: hwikim@korea.ac.kr
H.-S. Lee
Major of Electrical Engineering
College of Engineering
Pukyong National University
Yongso-ro, Busan, Nam-gu 48513, Republic of Korea
E-mail: lhs12100@pknu.ac.kr

The ORCID identification number(s) for the author(s) of this article can be found under https://doi.org/10.1002/lpor.202400080

© 2024 The Authors. Laser & Photonics Reviews published by Wiley-VCH GmbH. This is an open access article under the terms of the Creative Commons Attribution License, which permits use, distribution and reproduction in any medium, provided the original work is properly cited.

DOI: 10.1002/lpor.202400080

In addition, strong needs for complex SLM technology have arisen in a range of emerging wave-optic technology and applications such as light detection and ranging (LiDAR) sensors,[10] biology and medicine,[11] optical communications,[12] all-optical deep neural networks,[13] photonic quantum information processing,[14] as well as holographic 3D displays.[1–9,15]

The light modulation capabilities of SLMs can be characterized in the complex domain. The dynamic modulation range of an ideal complex SLM is represented by a unit circle. The zero-to-one amplitude and full 2π phase modulation ranges fill the unit circle completely in the complex domain. However, conventional SLMs have a limited modulation range, which is represented by a one-dimensional curve or line in the complex plane. Those of conventional amplitude-only SLMs and phase-only SLMs correspond to a partial line in the real axis and the circumference of a circle, respectively. In particular, those limited SLM modulations result in severe DC and conjugate noise[4] in holographic image generation. The optical noise can be suppressed if the dynamic range of the SLM is extended toward the 2D shape in the complex plane, however, this is possible when higher degrees of freedom are secured in the pixel-level modulation. One approach for the pixel-level complex modulation is layered SLMs, which vertically combine amplitude-only and phase-only SLMs,[4–6] wherein the modulation of an individual pixel can take the form of $A\exp(j\phi)$. However, the heterogenity of the amplitude-only and phase-only SLMs renders the resulting structures impractical. Recently, a more customized dual-layer approach has been proposed in the form of a double layer of identical in-plane switching (IPS) liquid crystal panels.[6] In practice, the dual-layer architecture is susceptible to various misalignment factors leading to low modulation efficiency and high inter-pixel crosstalk. Highly efficient and robust one-to-one vertical pixel interconnection between the upper and lower SLM panels is difficult to achieve with conventional fabrication techniques. An alternative approach is a complex macropixel composition. This method gathers a few adjacent normal pixels on a single panel for the alignment-free group interference action of its subpixels and makes them work together as an effective complex pixel at the cost of resolution.[1,3,4] In this case, optical noise is highly dependent on the macro pixel-topology. Accordingly, optimal macropixel topology design is an important issue for noise minimization without further loss of resolution.

In this paper, the optimal design for a novel macropixel topology for the single panel complex SLM, the three-phase covalent macropixel (3PCMP), is proposed. The design of the 3PCMP is based on our finding that point-symmetry in the macropixel is critical for low-noise complex field synthesis. To verify the proposed concept, a prototype of a slim complex SLM utilizing a single-panel amplitude-only liquid crystal display (LCD) is implemented, and its complex field synthesis performance is analyzed numerically and experimentally. The analysis reveals that the point symmetry in the macropixel topology is a key design factor to not only reduce optical noise but also enhance optical efficiency. Experimentally, the point symmetric macropixel can enhance the optical efficiency of holographic displays three times more compared to the conventional amplitude-only SLM-based holographic displays.

2. Results

2.1. Design of Three-Phase Covalent Macropixel

The proposed 3PCMP holographic display is schematically presented in **Figure 1**a. The 3PCMP SLM of the holographic display consists of an amplitude LCD of $H \times V$ resolution and a phase plate precisely aligned on the LCD panel. It is assumed that the eye of the viewer observes the 3D holographic image displayed by the 3PCMP holographic display. The 3D image observation of the holographic display is modeled by the cascade Fresnel transform (Supporting Information). As depicted in Figure 1a, the 3PCMP is composed of 2×2 amplitude subpixels and a 2×2 phase retarder. The 2×2 unit of the phase retarder consists of two 0° cells in the diagonal positions, and 120° and 240° phase retardation cells in the off-diagonal positions, respectively.

The amplitude transmittance of the (m, n)th macropixel is encoded by $A'_{m,n}$, $B'_{m,n}$, $C'_{m,n}$, and $D'_{m,n}$. Then, the complex transmittances of the macropixel are obtained by $A'_{m,n}$, $B'_{m,n}e^{j120^\circ}$, $C'_{m,n}e^{j240^\circ}$, and $D'_{m,n}$, respectively. The diffraction field of the single 3PCMP obtained at the pupil plane is approximately equal to the diffraction field of a single pixel of a complex amplitude $\eta_{m,n}$. $\eta_{m,n}$ is represented by the complex transmittances as

$$\eta_{m,n} = 2\left(A'_{m,n}/2\right) + B'_{m,n}e^{j120^\circ} + C'_{m,n}e^{j240^\circ} \tag{1}$$

The unique aspect of the 3PCMP is that its topology can be interpreted as the covalent overlap integration of three-phase symmetric macropixel (3PSMP) topology. The 3PSMP is the 3×3 point-symmetric topology as shown in Figure 1b. Its 3×3 topology is based on the complex number decomposition of $\eta_{m,n}$ into nine subpixel terms given as[16]

$$\eta_{m,n} = 5\left(A_{m,n}/5\right) + 2\left(B_{m,n}/2\right)e^{j120^\circ} + 2\left(C_{m,n}/2\right)e^{j240^\circ} \tag{2}$$

As seen in Figure 1b, in the 3PSMP, the real amplitude value of $A_{m,n}/5$ is encoded to the center and the four corners of the 3×3 pixel matrix, while the complex value of $B_{m,n}e^{j120^\circ}/2$ is encoded to the upper and lower rows in the center column, and $C_{m,n}e^{j240^\circ}/2$ is encoded to the left and right columns in the center row. The macropixel density of the 3PSMP reduces to $1/3 \times 1/3$ of the LCD panel, meaning the effective resolution of the 3PSMP SLM is $1/3(H) \times 1/3(V)$. Although the 3PSMP keeps the point-symmetry in the topological point of view, the issue is a high loss of resolution. The 3PCMP is to mitigate the cost of the resolution reduction without loss of point symmetry. Let us refer to the sharing of common columns and rows of the same phase encoding among adjacent macropixels as the covalent concatenation process. The covalent concatenation process squeezes the 3×3 3PSMP macropixel to a 2×2 3PCMP macropixel without loss of information and the point symmetry as depicted in Figure 1c.

Consider the 3PSMP topology shown in the left panel of Figure 1c. The (m, n)th macropixel at the center position, $P_{m,n}$ is surrounded by eight other macropixels, and then it is observed that the phases in the rightmost column of macropixel $P_{m,n-1}$, encoded by 0°, 240°, and 0°, are identical to those in the leftmost column of macropixel $P_{m,n}$. Similarly, the first row of macropixel $P_{m,n}$, encoded by 0°, 120°, and 0°, matches the third row of the macropixel $P_{m-1,n}$. Likewise, the right column of macropixel $P_{m,n}$ corresponds to the left column of the macropixel $P_{m,n+1}$, and the third row of the macropixel $P_{m,n}$ is identical to the first row of the macropixel $P_{m+1,n}$. In the right panel of Figure 1c, the overlapped region is indicated by dashed lines. As shown in Figure 1d, the 2×2 amplitude modulation values of the 3PCMP topology, $A'_{m,n}$, $B'_{m,n}$, $C'_{m,n}$, and $D'_{m,n}$ are related to the amplitudes of the baseline 3PSMPs, $A_{m,n}$, $B_{m,n}$, $C_{m,n}$, and $D_{m,n}$ as follows:

$$\begin{aligned}\left(A'_{m,n}, B'_{m,n}, C'_{m,n}, D'_{m,n}\right) &= \left(\sum_{k=-1}^{0}\sum_{l=-1}^{0}\frac{A_{(m+k,n+l)}}{5}, \sum_{k=-1}^{0}\frac{B_{(m+k,n)}}{2}e^{j120}, \right.\\ &\left. \times \sum_{k=-1}^{0}\frac{C(m,n+k)}{2}e^{j240}, \frac{A(m,n)}{5}\right)\end{aligned} \tag{3}$$

Through this encoding method, the rectangular array of 3PSMP is transformed into the covalently concatenated 3PCMP array. In practice, the 3PCMP simplifies the configuration of the arrangement of the phases. The subpixels with 0° and 120° phase alternate in the horizontal direction, while the subpixels with 0° and 240° phase alternate in the vertical direction. These straightforward arrangements facilitate the phase plate patterning more conveniently. The covalent macropixel formation process is a structural and geometric process without the dependency on wavelengths. In practice, the wavelength dependent phase-detuning issue can arise associated with the phase retardation device used in the implementation of 3PCMP. It will be shown in the later part that this issue can be resolved effectively.

To verify the performance of the 3PCMP in holographic 3D image generation, the 3PCMP topology is compared with other pixel topologies, a three-phase asymmetric macropixel (3PAMP) and 3PSMP, in terms of signal-to-noise ratio at the viewer's pupil plane and the quality of the 3D computer-generated hologram (CGH) image in **Figure 2**. The 3PAMP is the conventional macropixel structure without topological point symmetry.

Let the complex optical field at the 3PAMP SLM be denoted by $F_\lambda(x, y)$. The complex field distributions at the 3PSMP SLM panel and the 3PCMP SLM panel are denoted by $H_\lambda(x, y)$ and $T_\lambda(x, y)$,

© 2024 The Authors. Laser & Photonics Reviews published by Wiley-VCH GmbH

18638899, 0, Downloaded from https://onlinelibrary.wiley.com/doi/10.1002/lpor.202400080 by Korea University Library, Wiley Online Library on [09/05/2024]. See the Terms and Conditions (https://onlinelibrary.wiley.com/terms-and-conditions) on Wiley Online Library for rules of use; OA articles are governed by the applicable Creative Commons License

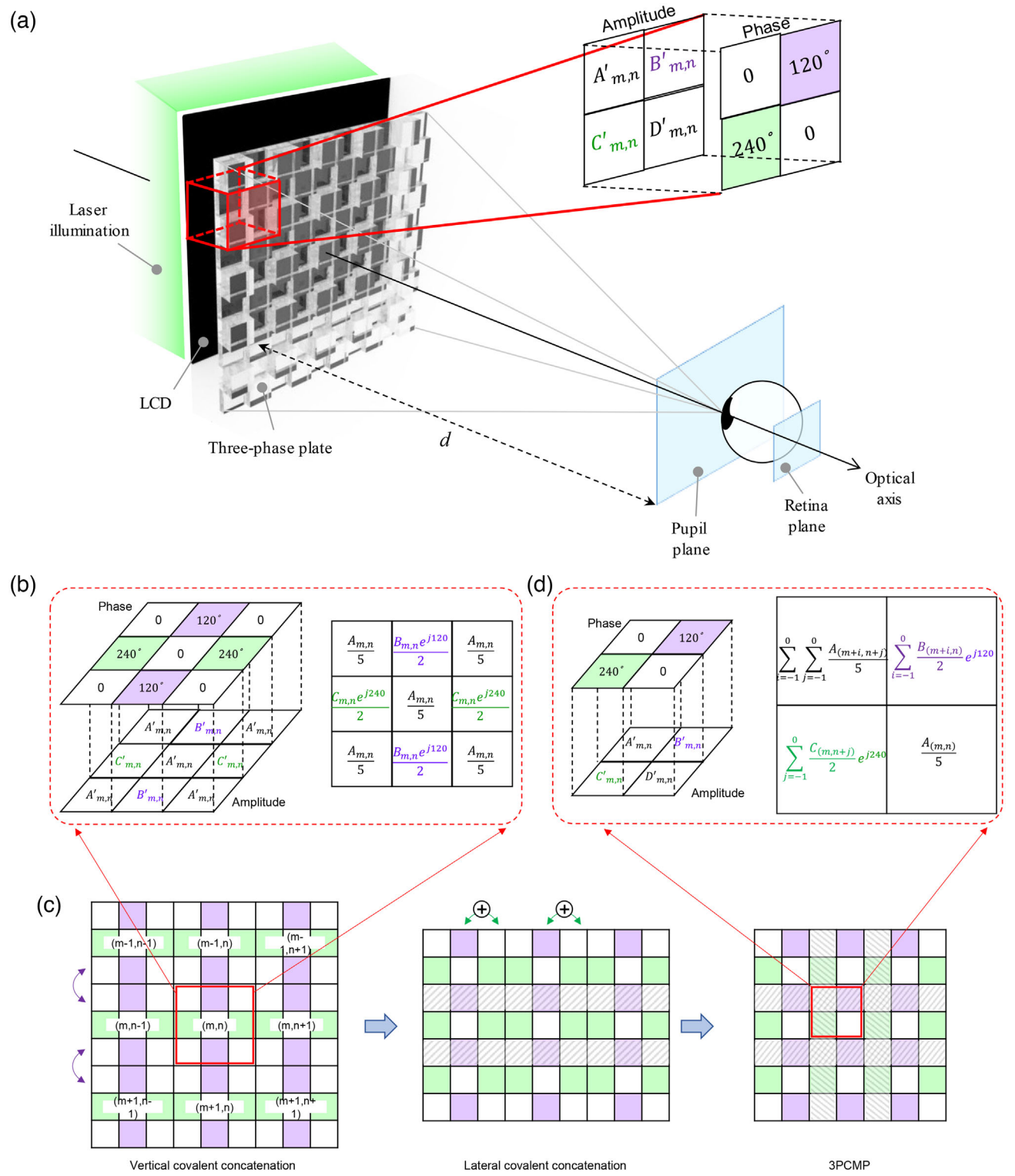

Figure 1. a) Schematic of the three-phase covalent macropixel (3PCMP) holographic display and the macro pixel topology. Complex spatial light modulator that consists of an LCD panel and a three-phase phase retardation plate, and transformation of b) three-phase point symmetric macropixel topology (3PSMP) to d) the proposed 3PCMP topology through c) the covalent concatenation process.

© 2024 The Authors. Laser & Photonics Reviews published by Wiley-VCH GmbH

18638899, 0, Downloaded from https://onlinelibrary.wiley.com/doi/10.1002/lpor.202400080 by Korea University Library, Wiley Online Library on [09/05/2024]. See the Terms and Conditions (https://onlinelibrary.wiley.com/terms-and-conditions) on Wiley Online Library for rules of use; OA articles are governed by the applicable Creative Commons License

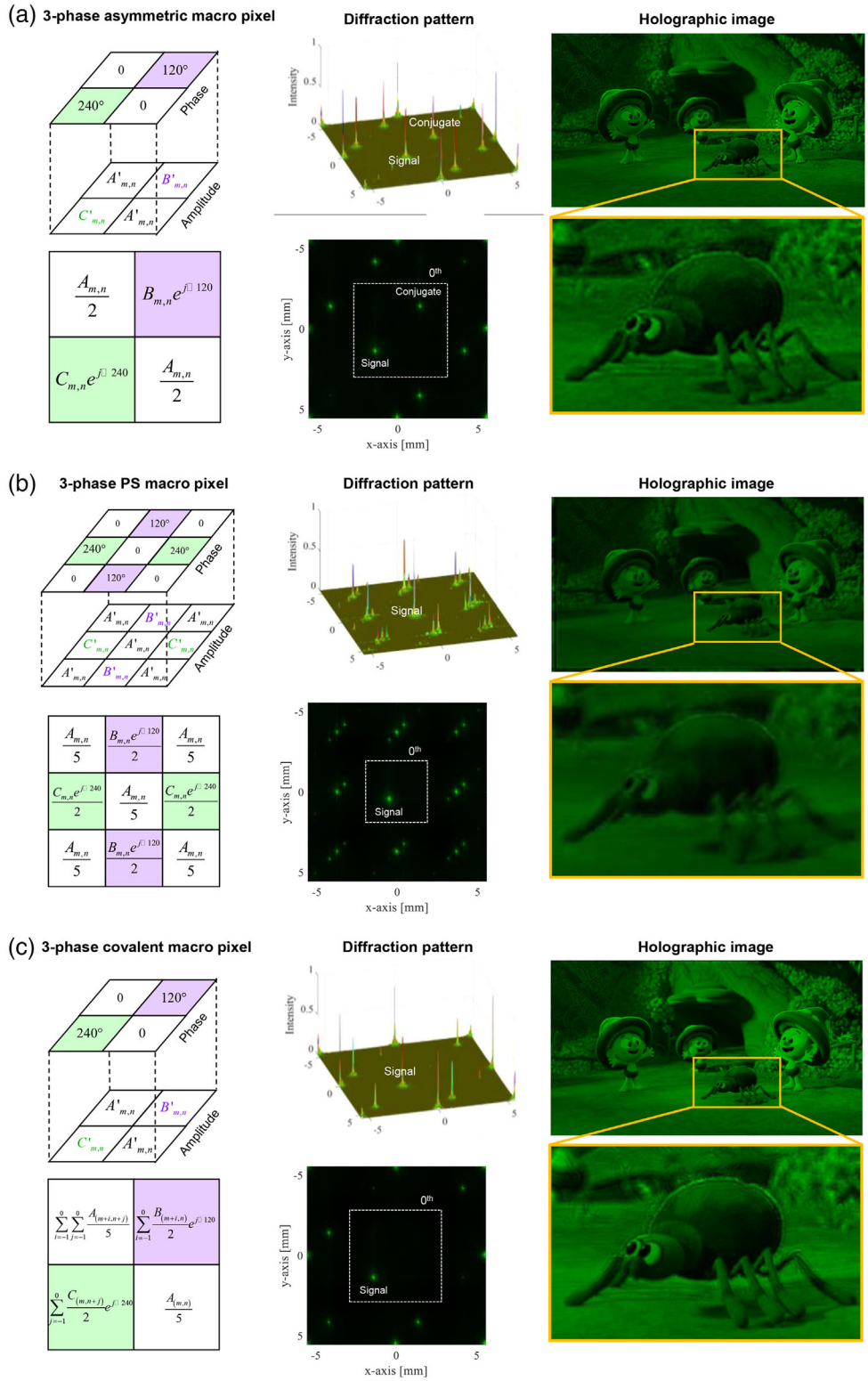

Figure 2. Numerical comparison of the macropixel units with respect to their diffraction pattern at the viewing zone and holographic image generation. The macropixel transmittance (left panel), diffraction patterns at the pupil plane including signal, DC, and conjugate terms (middle panel), and observed holographic images (right panel) of a) three-phase asymmetric macropixel (3PAMP), b) three-phase symmetric macropixel (3PSMP), and c) three-phase covalent macropixel (3PCMP) structures.

© 2024 The Authors. Laser & Photonics Reviews published by Wiley-VCH GmbH

18638899, 0, Downloaded from https://onlinelibrary.wiley.com/doi/10.1002/lpor.202400080 by Korea University Library, Wiley Online Library on [09/05/2024]. See the Terms and Conditions (https://onlinelibrary.wiley.com/terms-and-conditions) on Wiley Online Library for rules of use; OA articles are governed by the applicable Creative Commons License

respectively. The diffraction field distribution at the pupil plane for each case is modeled by the Fresnel transform as

$$\tilde{F}_{\lambda}(u,v) = Fr\{F_{\lambda}(x,y);d,\lambda\}, \text{ for 3PAMP} \quad (4)$$

$$\tilde{H}_{\lambda}(u,v) = Fr\{H_{\lambda}(x,y);d,\lambda\}, \text{ for 3PSMP} \quad (5)$$

$$\tilde{T}_{\lambda}(u,v) = Fr\{T_{\lambda}(x,y);d,\lambda\}, \text{ for 3PCMP} \quad (6)$$

where $Fr\{\cdot\}$ is the Fresnel transform. The holographic image fields in the retina plane of the viewer are modeled by the cascaded Fresnel transform as[17]

$$\bar{F}_{\lambda}(\bar{x},\bar{y}) = CdFr\{F_{\lambda}(x,y);d,f_d,\rho\}, \text{ for 3PAMP} \quad (7)$$

$$\bar{H}_{\lambda}(\bar{x},\bar{y}) = CdFr\{H_{\lambda}(x,y);d,f_d,\rho\}, \text{ for 3PSMP} \quad (8)$$

$$\bar{T}_{\lambda}(\bar{x},\bar{y}) = CdFr\{T_{\lambda}(x,y);d,f_d,\rho\}, \text{ for 3PCMP} \quad (9)$$

where $CdFr\{\cdot\}$ is the cascaded Fresnel transform (Supporting Information) and, f_d and ρ are the eye-lens focus and the radius of the eye pupil, respectively.

Figure 2a presents the diffraction field distribution in the viewer's pupil plane and its generated holographic image for the 3PAMP at the green wavelength (λ_g = 520 nm). The left panel illustrates the structure of 3PAMP with $A_{m,n}$, $B_{m,n}$, and $C_{m,n}$ encoded by the three-phase decomposition of $\eta_{m,n}$;

$$\eta_{m,n} = 2\left(A_{m,n}/2\right) + B_{m,n}e^{j120^{\circ}} + C_{m,n}e^{j240^{\circ}} \quad (10)$$

The middle and right panels in Figure 2a present the optical field distribution $\tilde{F}_{\lambda}(u,v)$ at the pupil plane and the holographic image $\bar{F}_{\lambda}(\bar{x},\bar{y})$ formed in the retinal plane. The complex field distributions at the 3PSMP SLM panel and the 3PCMP SLM panel are presented in Figure 2b,c, respectively. The numerical result shows that the point-symmetric macropixels (3PSMP and 3PCMP) reduce the DC and conjugate noise significantly in the pupil plane, while, in the case of 3PAMP without point symmetry, conjugate noise is clearly observed. This result manifests that maintaining point symmetry is essential for the generation of a pure complex signal field distribution without DC and conjugate noise contamination. The square dashed line in the pupil plane represents the 0^{th} viewing zone. The viewing zone of the 3PSMP SLM is smaller than that of the 3PAMP SLM because the size of the 3PSMP unit is larger than that of the 3PAMP unit. The right panels of Figure 2 compare the holographic images generated by the three macropixel topologies. It is observed that the resolution of the spider image for the 3PSMP topology shown in Figure 2b is lower than that for the 3PCMP topology shown in Figure 2c. For detailed comparison, parts of the holographic images of the 3PAMP and the 3PCMT are enlarged in **Figure 3**. The holographic image is reconstructed to be focused on the spider's eye. A closer examination of the eyes reveals that the 3PCMP provides a sharper image than the 3PAMP.

To quantitatively compare noise reduction, the diffraction field distributions in the pupil plane obtained in the numerical simulation (Figure 2) are analyzed. Assuming that the total power reaching the 0th viewing zone is 100%, the signal, DC noise, and conjugate noise power percentage ratios are tabulated in **Table 1**. The noise-to-signal ratios are calculated as a performance indicator.

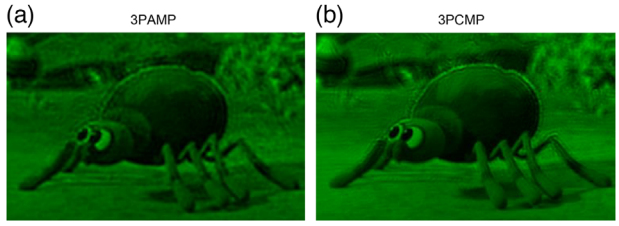

Figure 3. Comparison of the holographic images of the 3PAMP (3-phase asymmetric macro pixel) and point-symmetric 3PCMP (3-phase covalent macro pixel) SLMs. The magnified part of the spider in the holographic images generated by a) the 3PAMP SLM and b) the 3PCMP SLM.

In the case of the conventional amplitude-only SLM, nearly half of the total power (45%) is devoted to DC noise, while the other half is evenly divided into signal (27.7%) and conjugate (27.7%) terms. The DC noise-to-signal ratio is 161%. In contrast, using complex holographic displays (3PAMP, 3PSMP, and 3PCMP) results in a significant decrease in the noise-to-signal ratios and an absolute increase in signal power. It is apparent that the signal power ratio is highly dependent on macropixel topology. The 3PCMP shows the highest signal power ratio (99.7%), while the signal power ratio of the 3PAMP is just 60.6%. The conjugate noise of the 3PCMP (0.002%) is incomparably smaller than that of the 3PAMP (65%). This superiority of the 3PCMP in noise damping is ascribed to its topological point symmetry.

2.2. Experimental Results

A prototype of the 3PCMP SLM is implemented using a 5.5-inch size commercial full-color LCD panel (LCD model# LS055R1SX04 produced by Sharp Co.). The resolution of the LCD panel is QHD, 2560 (V) × 1440 (H) and the pixel pitch is 47.25 μm. It should be noted that the LCD panel employed in the prototype (Sharp LCD panel with QHD, 2560 (H) × 1440 (V)) has a 180°-phase difference between the pixel transmittances of the odd and even columns. To adjust the default phase retardation to zero point, the compensating phase retardation of 180° was added to the odd columns of the phase retardation plate at the green color (**Figure 4a**). The 2 × 2 phase plate is encoded by 0°, 60°, 120°, and 180° on the LCD panel with built-in 180° phase delay in the odd columns, then the 2 × 2 phase retardations of 0°, 120°, 240°, and 0° are obtained.

Figure 4a presents the experimental setup for holographic image generation with an inset image of the 3PCMP SLM. For a color light source, a Necsel RGB Novalum 1200 laser was used (λ_r = 638 nm, λ_g = 520 nm, λ_b = 465 nm). Behind the 3PCMP SLM is a 10-inch field lens with a focal length of 500 mm, which concentrates the diffracted field with holographic information to the viewing zone of the pupil plane. The field of view (FOV) of this system is estimated by 7.9°. The holographic image is captured by a color charge-coupled camera (CCD) (FLIR GS2-U3-120S6C-C, 4096 (H) × 3000 (V) pixels). The phase retardation plate presented in Figure 4b is fabricated on a glass substrate and precisely bonded to the SLM panel. During the alignment and bonding process of the phase plate to the LCD panel, various types of misalignments such as transpositions and rotations can occur.

© 2024 The Authors. Laser & Photonics Reviews published by Wiley-VCH GmbH

18638899, 0, Downloaded from https://onlinelibrary.wiley.com/doi/10.1002/lpor.202400080 by Korea University Library, Wiley Online Library on [09/05/2024]. See the Terms and Conditions (https://onlinelibrary.wiley.com/terms-and-conditions) on Wiley Online Library for rules of use; OA articles are governed by the applicable Creative Commons License

Table 1. Power ratios of signal, DC, and conjugate noise terms and the noise to signal ratio of the diffraction field by method: the macropixel topologies 3PAMP, 3PSMP, 3PCMP, and amplitude-only pixel.

Results Method	Ratio of Power [%]			Noise to Signal [%]		Resolution
	Signal	DC	Conjugate	DC/Sig	Con/Sig	
3PAMP	60.6	0.04	39.4	0.1	65	N/2(H) × N/2(V)
3PSMP	99.4	0.4	0.2	0.4	0.2	N/3(H) × N/3(V)
3PCMP	99.7	0.1	0.2	0.001	0.002	N/2(H) × N/2(V)
Amplitude-only	27.7	45	27.7	161	100	N(H) × N(V)

The misalignments between the phase retardation unit and the LCD pixels introduce noise into the system. Also, errors in the surface relief height introduced during the fabrication process can cause DC and conjugate noise. To mitigate alignment deviation, the surface relief side of the phase retardation plate is bonded to the LCD, minimizing the gap between the LCD pixels and the phase plate. The inset of Figure 4a shows a magnified micrograph image of the 3PCMP after the optical bonding of the phase plate and the LCD. The yellow rectangle area indicates a point-symmetric single 3PCMP unit. The angle written on a pixel is the total phase retardation at that pixel. The diffraction field distribution at the 0th viewing zone of the pupil plane is measured (**Figure** 5a) and the holographic image captured by the CCD is presented in Figure 5b. For the prototype of the 3PCMP SLM, the viewing zone size is 5.5(H) mm × 5.5(V) mm, and a highly enhanced signal spot and drastically suppressed conjugate and DC spots are observed.

The experiment proceeds to full color holographic image generation. For the full color CGH demonstration, the color-dependence compensation is devised. The red, green, and blue primary color lasers produce the full-color holographic field at the retina plane, which is represernted as

$$T_{RGB}(\bar{x},\bar{y}) = T_{\lambda_r}(\bar{x},\bar{y}) + T_{\lambda_g}(\bar{x},\bar{y}) + T_{\lambda_b}(\bar{x},\bar{y}) \tag{11}$$

In our prototype, the phase retardation plate is made in the form of surface relief grating with a three-phase retardation in 120° phase step at the green color ($\lambda_g = 520$ nm) as illustrated in Figure 1a. However, at red ($\lambda_r = 638$ nm) and blue ($\lambda_b = 473$ nm) colors, the phase retardation deviates from the designed value

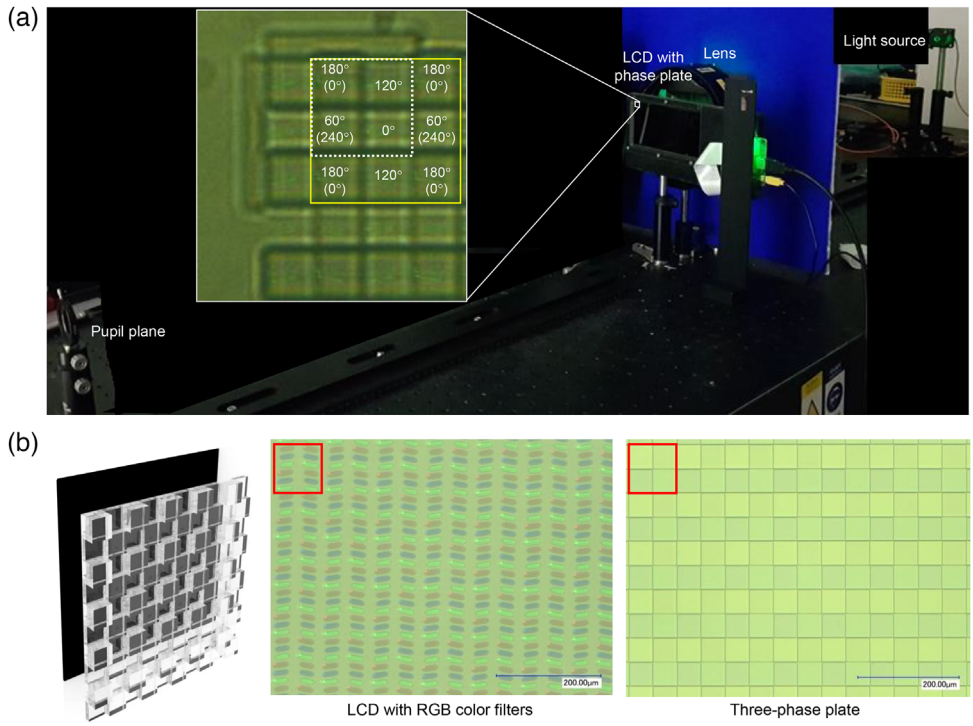

Figure 4. Prototype of the 3PCMP holographic display. a) Experimental setup consisting of the complex SLM prototype, a field lens, and a light source. The yellow line in the top left photomicrograph (500× magnification) of phase plate on LCD indicates one 3PCMP unit. The white dotted line shows one period of 3PCMP. The angle represents each phase of the phase plate, and the angle in parentheses are total phase considering the phase of the panel. b) 3PCMP SLM architecture, comprising an LCD panel and a phase plate, with 500× magnification micrographs showing pixels with the color filters on the LCD and the fabricated phase plate.

© 2024 The Authors. Laser & Photonics Reviews published by Wiley-VCH GmbH

18638899, 0, Downloaded from https://onlinelibrary.wiley.com/doi/10.1002/lpor.202400080 by Korea University Library, Wiley Online Library on [09/05/2024]. See the Terms and Conditions (https://onlinelibrary.wiley.com/terms-and-conditions) on Wiley Online Library for rules of use; OA articles are governed by the applicable Creative Commons License

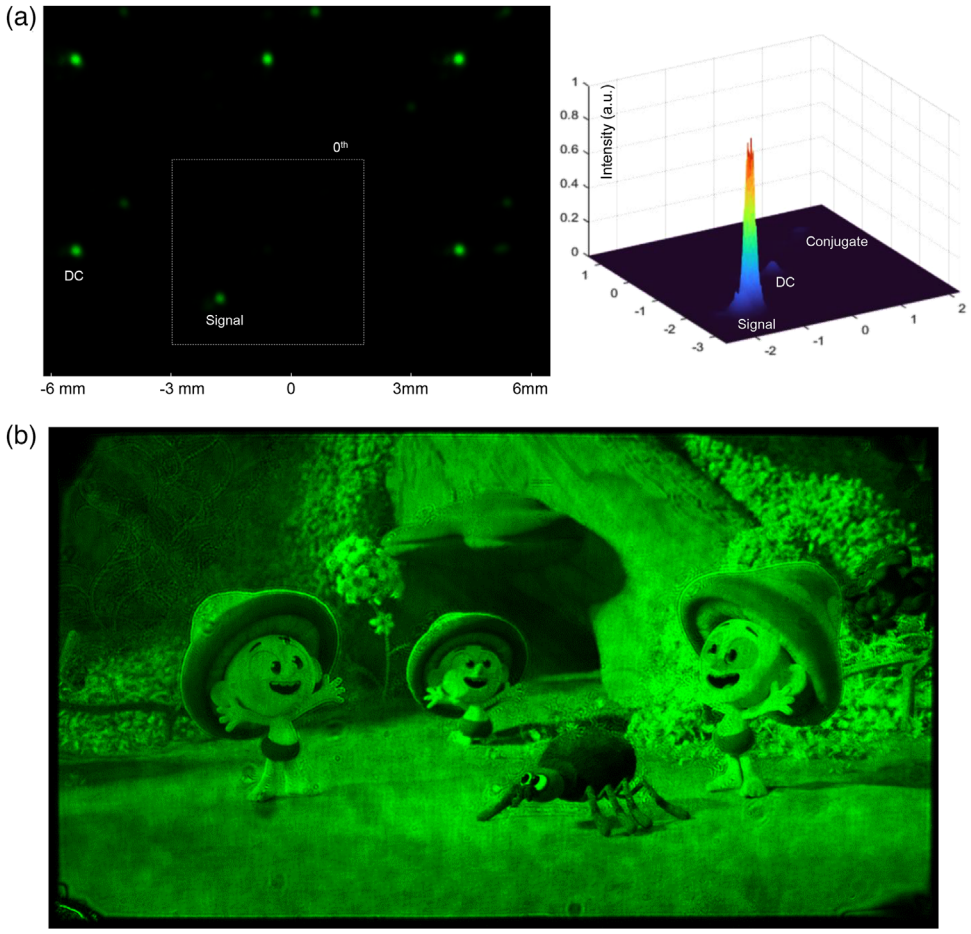

Figure 5. Experimental results showing a monocular complex holographic image displayed by the proposed complex holographic display. a) The diffraction pattern of the proposed complex hologram on the viewing zone plane and b) the observed holographic image.

due to the color-dependent phase modulation of the surface relief phase plate. Therefore, for the optimal design of full-color complex CGH, in this color-dependent architecture, a chormatic dispersion compensation method should be devised. Here, the Phase Basis Adjusting (PBA) algorithm is developed. The PBA algorithm encodes the full-color complex CGH taking into account the sets of phase retardation bases for red, green, and blue colors. The PBA algorithm considers that for the red wavelength λ_r, the phase retardation is given by $\theta_r = \theta_g \lambda_g / \lambda_r + \pi$ at the odd column and $\theta_r = \theta_g \lambda_g / \lambda_r$ at the even column. As a result, four-phase retardation bases are generated in the 2 × 2 phase plate unit as shown in **Figure 6**.

The PBA algorithm encodes the complex modulation $\eta_{m,n}$ by the four-component decomposition (Figure 6c),

$$\eta_{m,n} = A_{m,n} e^{j\theta_{r,0}} + B_{m,n} e^{j\theta_{r,1}} + C_{m,n} e^{j\theta_{r,2}} + D_{m,n} e^{j\theta_{r,3}} \quad (12)$$

where $\theta_{r,0}$, $\theta_{r,1}$, $\theta_{r,2}$, and $\theta_{r,3}$ denote the four-phase bases obtained for red color. In the same manner, the PBA algorithm is applied to encode the blue component CGH with the phase basis split into four phase bases. It should be noted that, although the phase bases for red and blue colors are split into four bases, the 3PCMP topology still preserves point-symmetry. For instance, consider the neighboring macropixels around the (m, n)th macropixel (Figure 1d) in red color. The four subpixels with 327° phase retardation of the (m, n), (m, n+1), (m+1, n), and (m+1, n+1) macropixels are arranged with point symmetry around the subpixel with 0° phase of the (m, n) macropixel. Similarly, two subpixels with 98° phase retardation (along the vertical direction) and two subpixels with 229° phase retardation (along the horizontal direction) also conserve point symmetry in the 3PCMP topology (Figure 1d). Thus, the PBA algorithm allows the 3PCMP to properly work for primary red, green, and blue colors. **Figure 7** presents a simulation of the optical noise generation for the red, green, and blue components of the color CGH encoded by the PBA. The power ratio of signal, DC, and conjugate obtained in the numerical simulation are summarized in **Table 2**. The ratio of the conjugate noise to the signal remains quite small for all colors. In the case without the PBA, there is considerable DC noise in red and blue colors. The blue DC (1.3%) is smaller than the red DC (4.5%). With the PBA applied, as seen in Figure 7b, DC is drastically reduced to near zero, being unperceivable in the viewing zone for all colors.

Figure 8 presents a full-color complex holographic image displayed by the 3PCMP SLM. In the holographic image, the yellow flowers and the spider are placed at different depths, which are

© 2024 The Authors. Laser & Photonics Reviews published by Wiley-VCH GmbH

18638899, 0, Downloaded from https://onlinelibrary.wiley.com/doi/10.1002/lpor.202400080 by Korea University Library, Wiley Online Library on [09/05/2024]. See the Terms and Conditions (https://onlinelibrary.wiley.com/terms-and-conditions) on Wiley Online Library for rules of use; OA articles are governed by the applicable Creative Commons License

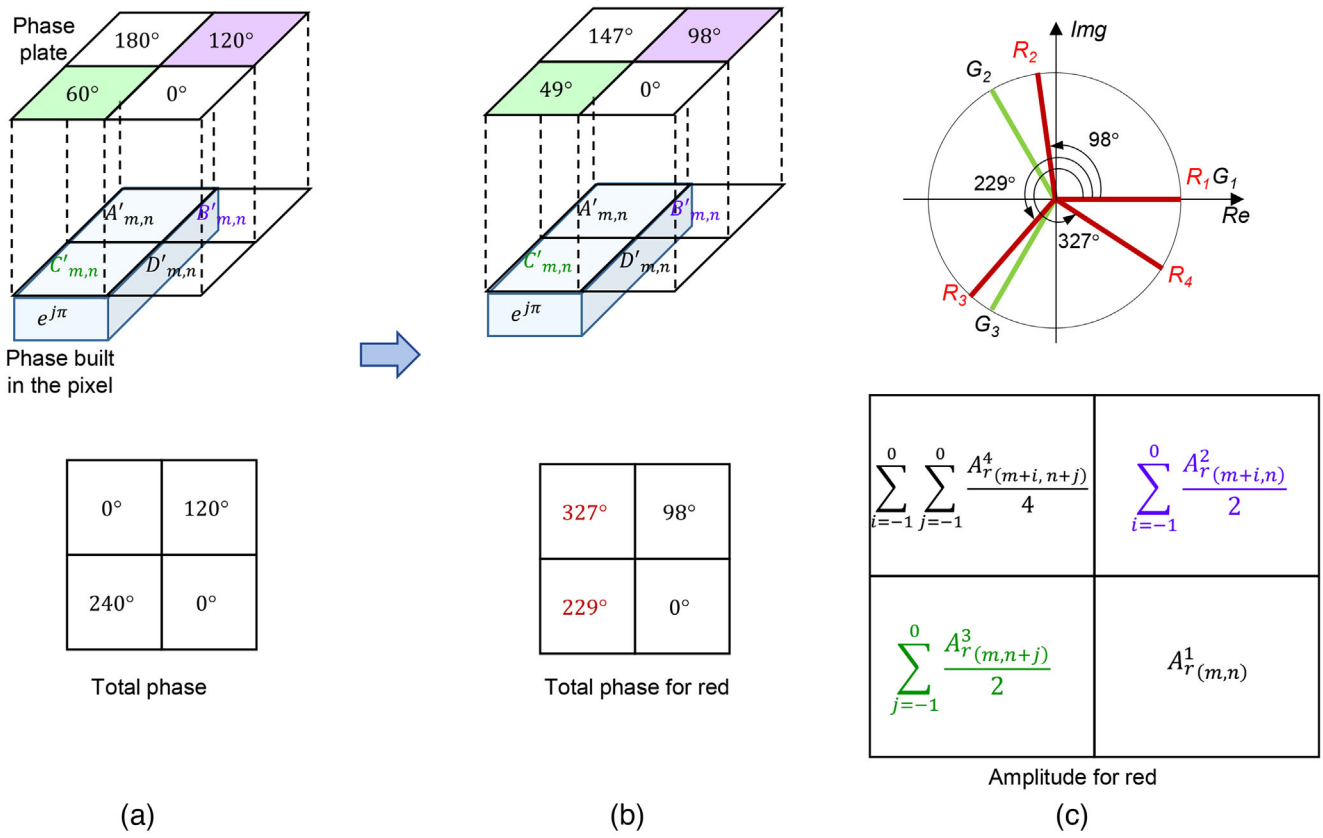

Figure 6. Phase-basis adjustment (PBA) algorithm for color complex modulation. a) Optical transmittance of the green color phase plate, b) optical transmittance of the red color phase plate, and c) the amplitude encoding scheme with corrected four-phase-basis plate.

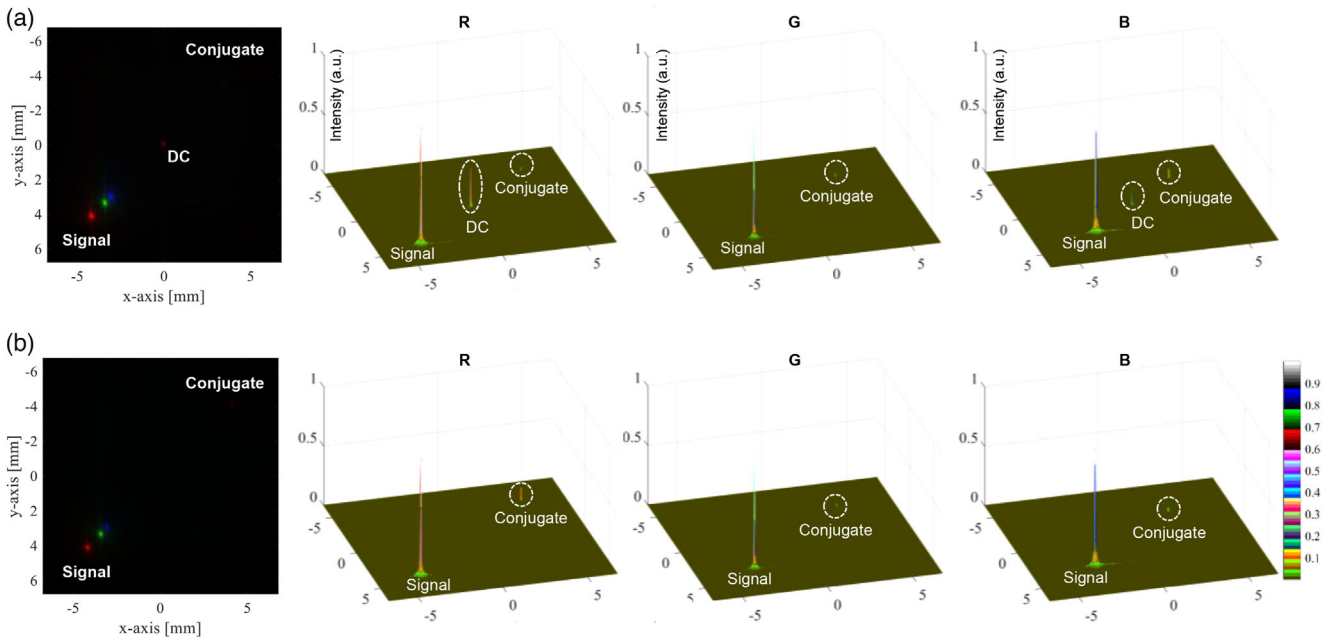

Figure 7. Numerical comparison of the diffraction patterns in the pupil plane in the full-color holographic image generation of the 3PCMP SLM. Diffraction field distributions obtained a) without and b) with using the phase-basis adjustment (PBA) algorithm according to the colors. The wavelength for red is 638 nm, green is 520 nm, and blue is 473 nm. The intensity values of the diffraction patterns are summarized in Table 2.

© 2024 The Authors. Laser & Photonics Reviews published by Wiley-VCH GmbH

18638899, 0, Downloaded from https://onlinelibrary.wiley.com/doi/10.1002/lpor.202400080 by Korea University Library, Wiley Online Library on [09/05/2024]. See the Terms and Conditions (https://onlinelibrary.wiley.com/terms-and-conditions) on Wiley Online Library for rules of use; OA articles are governed by the applicable Creative Commons License

Table 2. Power ratios of signal, DC, and conjugate noise terms and noise-to-signal ratios in the diffracted fields at the viewing zone for the 3PCMP SLM without and with the PBA algorithm applied.

Results Method		Ratio of Power [%]			Noise to Signal [%]	
		Signal	DC	Conjugate	DC/Sig	Con/Sig
WO/PBA	R	95.3	4.5	0.1	4.8	0.1
	G	99.7	0.1	0.2	0.1	0.2
	B	97.9	1.3	0.9	1.3	0.9
W/PBA	R	98.4	0.0	1.6	0.0	1.6
	G	99.7	0.1	0.2	0.1	0.2
	B	99.7	0.1	0.2	0.1	0.2

located 16 and 50 cm in front of the SLM panel, respectively. In Figure 8a,b, the accommodation effect is clearly observed such that, when the flowers are focused, the spider is out of focus, and vice versa. In the diffraction pattern in Figure 8c, the blue signal power recognized by the CCD is so weak as to be clearly perceived because it is adjusted to have a weak output to match the white balance of the holographic image. However, if you observe the Fairies' eyes or the white dots in their mushroom hats, the blue color is apparent in Figure 8 . The normalized field distributions in the pupil plane for each color component are shown in Figure 8d.

A quantitative analysis of the noise-to-signal power ratio is carried out for the diffraction field pattern in the viewing zone, as shown in Figure 8c,d. The total power of the 0th region is normalized to 100% for each color, and the relative power ratios of the DC, conjugate, and the signal components for each color are evaluated. The result of the analysis shown in **Table 3** reveals that the green signal reaches about 91%, while green DC and conjugate terms have 7% and 2% power ratios. For comparison, a conventional holographic display using an amplitude-only SLM is evaluated. The result is that the power of the green signal is 20%, as is the conjugate power, and DC has about 61% of the power rounded off. That is, the DC is three times stronger than either the signal or the conjugate.

In experimental measurement, the dynamic range of the CCD is limited to 256 levels, and care must be taken when measuring the diffracted light distribution to avoid saturating the maximum intensity value. In practice, the CCD saturation issue makes it

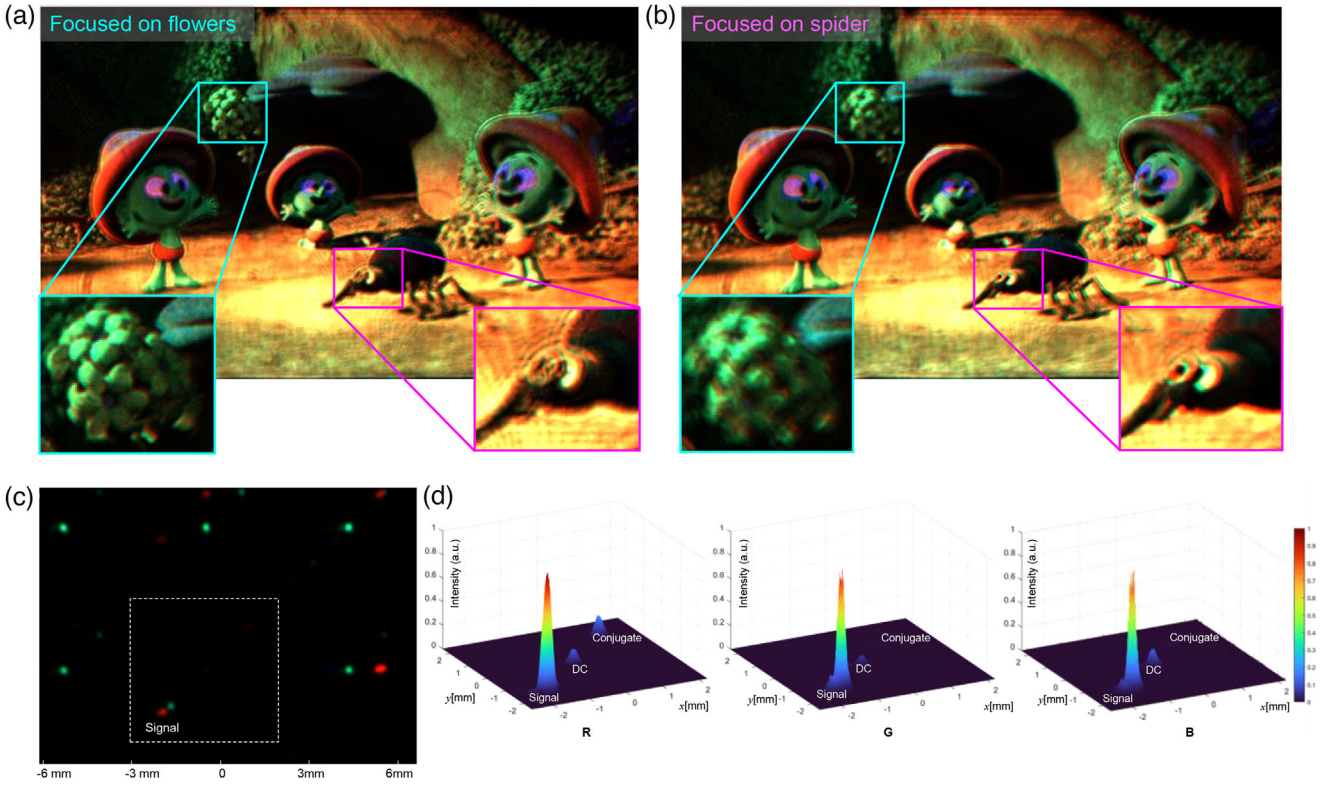

Figure 8. Experimental results showing a full-color complex holographic image displayed by the proposed complex holographic display. a) Image focused on yellow flowers, and b) image focused on the spider in the foreground. c) Full-color diffraction pattern captured at the viewing zone. The dashed line indicates the 0^{th} viewing zone and d) visualization results of the diffraction pattern in c) according to color.

© 2024 The Authors. Laser & Photonics Reviews published by Wiley-VCH GmbH

18638899, 0, Downloaded from https://onlinelibrary.wiley.com/doi/10.1002/lpor.202400080 by Korea University Library, Wiley Online Library on [09/05/2024]. See the Terms and Conditions (https://onlinelibrary.wiley.com/terms-and-conditions) on Wiley Online Library for rules of use; OA articles are governed by the applicable Creative Commons License

Table 3. Power ratios of signal, DC, and conjugate noise terms and noise to signal ratios in the diffracted fields at the viewing zone for the 3PCMP SLM.

Results Method		Ratio of Power [%]			Noise to Signal [%]	
		Signal	DC	Conjugate	DC/Sig	Con/Sig
3CMP	Green	91	7	2	8	2
	Red	79	9	12	12	15
	Blue	84	14	2	16	3
Amplitude-only		20	61	20	307	100

difficult to obtain precise noise measurements and may induce some errors. Comparing the experimental results in Table 3 to the simulation results in Table 2, the simulation results present a higher signal ratio (99.7%) than that of the experimental results (91%) at the green value. As already mentioned above, various types of fabrication errors occur, such as misalignment, and non-uniform bonding gaps. These misalignments prevent our prototype from achieving the ideal performance given by the numerical model. Since the phase plate and panel pixels have periodic patterns, in case the transposition alignment error is 1/2 of the LCD pixel, the imaging quality degradation is most severe and both DC and conjugate noises increase at the same time. While, if the error becomes one pixel, the image processing can correct the error to the same state as the perfect alignment. The acceptable maximum alignment error would be the black matrix width of the LCD. There are possible errors in rotation and tilting alignments. However, if the phase array is automatically processed to be attached during the top LCD manufacturing process, the error caused by the alignment is expected to be overcome.

In practice, the fabrication error can have more influence on the blue color component of shorter wavelength as presented in Table 3. Further optimization and enhancement of the fabrication process should be pursued. Nonetheless, significant improvements in both signal power and noise reduction are apparent using the proposed 3PCMP holographic display, and, overall, good agreement exists between the experimental and the numerical results. The DC and conjugate noise-to-signal ratios at green color are reduced to 1/38 and 1/50, respectively, compared to conventional holographic displays using amplitude-only SLMs. Thus, our experimental results have validated the effectiveness of our proposed method.

3. Conclusion

In this study, we have presented and demonstrated a full-complex holographic display as a step toward the ultimate holographic 3D display. The noise reduction principle of the point-symmetric macropixel is verified and the novel design of 3PCMP SLM is successfully demonstrated for the generation of full-complex color holographic images. The 3PCMP SLM extends the area over which the signal is available to the entire area of the 0th viewing zone, allowing the viewer to observe accurate holographic images without contamination by DC or conjugate noise in the expanded area of view. In this case, we can expect to display non-color-dispersion full-color CGH images, since we can display full-color CGH without the prism phase that is used for signal separation from DC and conjugate terms, forming the signal spots of RGB components at the center of the pupil plane. The 3PCMP leads to three times optical efficiency enhancement of the SLM for holographic image generation. The signal is quite bright compared even to higher-order DC, that is almost all the energy for the 0th viewing zone is concentrated on the signal, as proven not only by simulation results but also by experimental results. Moreover, the phase-sharing features of the 3PCMP structure and the algorithm not only simplify the phase arrangement but also contribute to high information density and image quality improvement. As a result, there is no need for additional bulky optical parts to filter noise, such as 4-f systems. The proposed method using the phase plates and the encoding algorithms forms a compact and slim filter for holographic display.[18] It is relatively easy to implement the 3PCMP SLM, utilizing commercially available off-the-shelf LCD panels and a thin fabricated phase plate. Overall, these features make our method practical and straightforward for use in real applications. This approach is also expected to contribute to the form factor miniaturization of holographic AR/VR glasses and more practical real-time complex CGH processing.[19] Also, this technique enables new technologies such as viewing zone expansion and high-performance eye tracking for holographic displays.

In constructing our prototype, we manually aligned and bonded the LCD to the phase plate. In order to minimize diffraction between the LCD and the phase plate, the uneven surface of the phase plate was turned over to the floor and bonded to the LCD. If the phase array is automatically attached during the top LCD manufacturing process, the error caused by the misalignment is expected to be overcome. We also presented a PBA algorithm to compensate for the phase difference according to the RGB colors, and proved the robustness of the full-color holographic image generation of our design using only a single phase retardation plate.

Alternatively, if an achromatic phase retardation plate is applied, full-color operation becomes possible without the need for the PBA algorithm. Constrained by the 120° phase step three-phase encoding for RGB wavelengths, the surface relief phase retardation plate must have at least seven-level steps for full-color operation, and this design may suffer from issues such as a high-cost multi-level fabrication process and alignment difficulties. The achromatic phase retardation plate will be able to overcome the limitations faced by current complex SLMs. Recently, the design of an in-cell phase retardation single-panel complex SLM was introduced.[20] The geometric phase retardation layer with achromatic phase modulation capability is embedded inside the amplitude-only SLM panel to perform full-color holographic image generation. Thus, the embedding of the geometric phase layer into the 3PCMP SLM can alleviate the

© 2024 The Authors. Laser & Photonics Reviews published by Wiley-VCH GmbH

18638899, 0, Downloaded from https://onlinelibrary.wiley.com/doi/10.1002/lpor.202400080 by Korea University Library, Wiley Online Library on [09/05/2024]. See the Terms and Conditions (https://onlinelibrary.wiley.com/terms-and-conditions) on Wiley Online Library for rules of use; OA articles are governed by the applicable Creative Commons License

alignment issues between the color pixels and the corresponding phase retardation layer and the related inter-layer crosstalk. Metasurface-based flat components are promising candidates for the geometric phase retarders, leveraging their excellence in broadband, high resolution, and large field of view at visible wavelengths. Various metasurface architectures have been introduced for complex spatial light modulation, which can significantly contribute to implementing highly efficient complex spatial light modulators in near future.[21–25] Additionally, higher-resolution display panel structures based on multi-vision tiling will resolve the issue of resolution deterioration for holographic 3D images. All results highlight the potential of the proposed method to advance holographic display technology. The proposed complex light modulation is expected to be widely used as a core technology in a wide range of applications including holographic displays, light detection and ranging sensors, imaging, lens-less photolithography, image sensors, all-optical complex neural networks, biology, and medicine.

4. Experimental Section

Fabrication of 3PCMP: The phase arrangement of the phase plate was designed using the proposed 3PCMP pixel topology. The phase plate was fabricated using patterned plasma-enhanced chemical vapor deposition (PECVD) silicon oxide layers on Eagle XG glass substrate. Prior to the main fabrication process, the thickness and reflective index were calibrated to minimize the diffracted power by the grating structure in phase π. A four-phase retardation, 0°, 60°, 120°, and 180°, was implemented for the green color. The main fabrication process was composed of PECVD oxide deposition, photoresist patterning, and oxide reactive ion etching (RIE). These processes were repeated three times to create the four phase levels. After the fabrication, the phase plate was aligned on the LCD panel using an assembled aligner. The aligner consisted of two microscopes, xyz micrometers, the LCD panel holder, and the plate holder with vacuum lines on the top and bottom, respectively. The alignment of the pixel and each phase was done manually using the aligner. Fine adjustment on the panel was crucial for accurate complex light modulation.

Computation and simulation of CGH: A wave optical field representation model was developed for CGH calculation used for both experiments and simulations, which included the Fresnel transform and cascaded Fresnel transform (Supporting Information). This tool was developed in MATLAB. To ensure consistency across the experiments, the CGH calculation conditions were set up as follows: a resolution of 2560 (V) × 1440 (H), pixel size of 47.25 μm, distance between CGH and eye-lens of 1 m, and distance between the eye-lens and retina of 25 mm. The simulation pixel model, based on the proposed pixel scheme, decomposed one complex pixel into subpixels. Consequently, during the simulation's reconstruction process, high-order diffraction can be observed in the signal distribution of the pupil plane. The values assigned to the subpixels can be calculated according to Equation (S4) (Supporting Information).

Supporting Information

Supporting Information is available from the Wiley Online Library or from the author.

Acknowledgements

This work was supported by Alchemist Project grant funded by Korea Evaluation Institute of Industrial Technology (KEIT) & the Korea Government (MOTIE) (Project Number: 1415185027, 20019169) and Samsung Electronics Co.

Conflict of Interest

The authors declare no conflict of interest.

Author Contributions

Y.K. and J.L. contributed equally to this work. H.K., Y.K., and J.L. conceived the idea, and Y.K. and J.L. performed the theoretical analysis. H.S. and Y.K. designed and performed the phase plate fabrication. Y.K., J.L., S.N., and S.K. conducted the numerical simulations. Y.K. and H.Y. performed the experiments and analyzed the experimental data. C.C, H.K., and J.A. post-processed the display panel and supported the use of color laser light sources for experiments. H.K. and H.-S.L. supervised the project. Y.K. and H.K. wrote the manuscript. All authors discussed the results and contributed to the manuscript.

Data Availability Statement

The data that support the findings of this study are available from the corresponding author upon reasonable request.

Keywords

complex spatial light modulator, computer-generated hologram, holographic display, three-phase covalent macro pixel

Received: January 17, 2024
Revised: March 25, 2024
Published online:

[1] S. Reichelt, R. Häussler, G. Fütterer, N. Leister, H. Kato, N. Usukura, Y. Kanbayashi, *Opt. Lett.* **2012**, *37*, 1955.
[2] H. Ren, X. Fang, J. Jang, J. Bürger, J. Rho, S. A. Maier, *Nat. nanotechnology* **2020**, *15*, 948.
[3] X. Guo, J. Zhong, B. Li, S. Qi, Y. Li, P. Li, D. Wen, S. Liu, B. Wei, J. Zhao, *Adv. Mater.* **2022**, *34*, 2103192.
[4] P. W. M. Tsang, T.-C. Poon, *IEEE Trans. Ind. Inform.* **2016**, *12*, 886.
[5] R. Tudela, E. Martin-Badosa, I. Labastida, S. Vallmitjana, I. Juvells, A. Carnicer, *J. Opt. A: Pure and Applied Optics* **2003**, *5*, S189.
[6] S.-W. Jang, W. Choi, S. Kim, J. Lee, S. Na, S. Ham, J. Park, H. Kang, B.-K. Ju, H. Kim, *Sci. Rep.* **2022**, *12*, 8277.
[7] J.-P. Liu, W.-Y. Hsieh, T.-C. Poon, P. Tsang, *Appl. Opt.* **2011**, *50*, H128.
[8] H. Kim, C.-Y. Hwang, K.-S. Kim, J. Roh, W. Moon, S. Kim, B.-R. Lee, S. Oh, J. Hahn, *Appl. Opt.* **2014**, *53*, G139.
[9] T. Shimobaba, T. Takahashi, Y. Yamamoto, I. Hoshi, A. Shiraki, T. Kakue, T. Ito, *J Opt* **2020**, *22*, 045703.
[10] J. Park, B. G. Jeong, S. I. Kim, D. Lee, J. Kim, C. Shin, C. B. Lee, T. Otsuka, J. Kyoung, S. Kim, *Nat. Nanotechnol.* **2021**, *16*, 69.
[11] J. A. Rodrigo, T. Alieva, *Optica* **2015**, *2*, 812.
[12] S. Ahderom, M. Raisi, K. Lo, K. E. Alameh, R. Mavaddat, in 5th IEEE International Conference on High Speed Networks and Multimedia Communication (Cat. No. 02EX612), IEEE, Piscataway, NJ **2002**, pp. 239–242.
[13] Y. Zuo, Y. Zhao, Y.-C. Chen, S. Du, J. Liu, *Phys. Rev. Applied* **2021**, *15*, 054034.
[14] K. H. Kagalwala, G. Di Giuseppe, A. F. Abouraddy, B. E. Saleh, *Nat. Commun.* **2017**, *8*, 739.
[15] D. Gabor, *Science* **1972**, *177*, 299.
[16] C. B. Burckhardt, *Appl. Opt.* **1970**, *9*, 1949.
[17] D. Im, E. Moon, Y. Park, D. Lee, J. Hahn, H. Kim, *Opt. Lett.* **2014**, *39*, 3642.
[18] J. An, K. Won, Y. Kim, J.-Y. Hong, H. Kim, Y. Kim, H. Song, C. Choi, Y. Kim, J. Seo, *Nat. Commun.* **2020**, *11*, 5568.

© 2024 The Authors. Laser & Photonics Reviews published by Wiley-VCH GmbH

18638899, 0, Downloaded from https://onlinelibrary.wiley.com/doi/10.1002/lpor.202400080 by Korea University Library, Wiley Online Library on [09/05/2024]. See the Terms and Conditions (https://onlinelibrary.wiley.com/terms-and-conditions) on Wiley Online Library for rules of use; OA articles are governed by the applicable Creative Commons License

[19] H. Kim, Y. Kim, H. Ji, H. Park, J. An, H. Song, Y. T. Kim, H.-S. Lee, K. Kim, *IEEE Trans Ind Electron* **2018**, *66*, 2066.
[20] S. Na, S. Kim, J. Lee, Y. Kim, H. Kim, *Opt. Lett.* **2022**, *47*, 5909.
[21] M. Khorasaninejad, F. Capasso, *Science* **2017**, *358*, eaam8100.
[22] G.-Y. Lee, J.-Y. Hong, S. Hwang, S. Moon, H. Kang, S. Jeon, H. Kim, J.-H. Jeong, B. Lee, *Nat. Commun.* **2018**, *9*, 4562.
[23] G.-Y. Lee, G. Yoon, S.-Y. Lee, H. Yun, J. Cho, K. Lee, H. Kim, J. Rho, B. Lee, *Nanoscale* **2018**, *10*, 4237.
[24] Z. Li, P. Lin, Y.-W. Huang, J.-S. Park, W. T. Chen, Z. Shi, C.-W. Qiu, J.-X. Cheng, F. Capasso, *Sci. Adv.* **2021**, *7*, eabe4458.
[25] C. Park, W. Kim, Y. Kim, H. Sung, J. Park, H. Song, J. Kim, D. K. Oh, H. Kang, N. Jeon, J. Rho, H. Lee, *Adv. Opt. Mater.* **2024**, 2301562.

© 2024 The Authors. Laser & Photonics Reviews published by Wiley-VCH GmbH

18638899, 0, Downloaded from https://onlinelibrary.wiley.com/doi/10.1002/lpor.202400080 by Korea University Library, Wiley Online Library on [09/05/2024]. See the Terms and Conditions (https://onlinelibrary.wiley.com/terms-and-conditions) on Wiley Online Library for rules of use; OA articles are governed by the applicable Creative Commons License